Atomic-resolution study of charge transfer effects at the LaTiO₃/LaFeO₃ interface

Chenyi Gu,[1,*] Min Gu,[1,*] Chunchen Zhang,[1] Zhoushen Yuan,[1] Zhengbin Gu ⓘ,[1] Jian Zhou ⓘ,[1] Yuefeng Nie,[1,†]
Peng Wang,[1,‡] and Xiaoqing Pan ⓘ[2]

[1]*National Laboratory of Solid State Microstructures, College of Engineering and Applied Sciences, and Collaborative Innovation
Center of Advanced Microstructures, Nanjing University, Nanjing 210093, China*

[2]*Department of Chemical Engineering and Materials Science and Department of Physics and Astronomy, University of California,
Irvine, 916 Engineering Tower, Irvine, California 92697, USA*

Charge transfer effect can give rise to exotic two-dimensional phenomena at not only polar-nonpolar interfaces but also isopolar interfaces in complex oxides. Here, we investigate the valence state changes of both Ti and Fe at the LaTiO₃/LaFeO₃ interface by a combination of density functional theory calculations, molecular beam epitaxy, and aberration-corrected scanning transmission electron microscopy. We demonstrate that the charge transfer from Ti to Fe occurs near the interface. The majority of the transferred charge is located within 1 unit cell from the interface. Our results present a detailed understanding of the interfacial charge transfer effect upon the design of functional oxide heterostructures.

I. INTRODUCTION

Transition metal oxides (TMOs) have gathered great attention in condensed matter physics for their properties originated from strongly correlated d electrons and the interplay between charge, spin, and orbital degrees of freedom [1]. Benefited from the recent advance in epitaxial growth technology [2], TMO multilayer heterostructures can now be synthesized with precision on the atomic level and with well-defined interfaces [3]. More importantly, these interfaces generate physical properties which are not found in the bulk of the constituting materials [4–6]. For instance, the interfaces between polar and nonpolar TMO films [i.e., LaAlO₃/SrTiO₃ (STO)] possess properties such as high-mobility two-dimensional electron gas, ferromagnetism, and the coexistence of magnetic order with two-dimensional superconductivity [7–9]. In addition, interfaces retaining polar continuity also exhibit exotic properties such as exchange bias and ferromagnetism [5,6]. The heterointerface between the Mott-Hubbard insulator LaTiO₃ (LTO) and the charge transfer insulator LaFeO₃ (LFO) is a prototype for the investigation of the charge transfer effect in oxides. Both materials are G-type antiferromagnetic in the bulk and have an orthorhombic structure with GdFeO₃-type distortion [10,11]. The isopolar LTO/LFO interface is different from the widely studied polar discontinued interfaces such as LaAlO₃/STO [7], providing perspective on electronic reconstruction without the complicated effect of polar catastrophe. Recently, a principle of predicting band alignment and charge transfer in oxide interfaces was established [12]. This principle is based on the continuity condition of the oxygen

$2p$ state at the interface since the interfacial oxygen atoms are shared by both constituents. Therefore, charge transfer at oxide interfaces can be well predicted by comparing the bulk values of the oxygen $2p$ band energy between the two constituents.

The previous study by Kleibeuker *et al.* [13] shows the electronic reconstruction at the interface between LTO and LFO. Their work revealed the valence state change of Fe at the interface by angle-dependent x-ray photoelectron spectroscopy, suggesting a possible charge transfer from Ti to Fe. An intriguing LFO magnetic ground state change from antiferromagnetic to nonmagnetic was also observed in their work. Unlike the observed Fe valence state change from +3 in the bulk to +2 at the interface, only a single state of ∼+4 was observed for Ti in the two-unit-cell-thick LTO, making this charge transfer scenario ambiguous. For example, it is possible to form the La₂Ti₂O₇ impurity phase during the growth of LTO film [14,15]. This can be one plausible reason for the deviation from Ti +3 and needs to be ruled out to establish the scenario of charge transfer from Ti to Fe. Moreover, though their study suggests that the charge transfer is limited near the interface, the layer-resolved distribution of the charge transfer has not been determined. To fully understand the charge transfer scenario at the LTO/LFO interface and to study the spatial distribution of the charge transfer effect at the atomic level, it is essential to experimentally investigate the valence state changes of both Ti and Fe unit cell by unit cell. With the development of spherical aberration correction technology, the performance of transmission electron microscopy (TEM) has been greatly improved in recent years [16–19]. As a result, the spatial resolution of a scanning TEM (STEM) has been pushed into the sub-Ångström regime [16]. Combining aberration-corrected STEM high-angle annular dark-field (HAADF) imaging, energy-dispersive x-ray spectroscopy (EDS), and electron energy loss spectroscopy

---

*These authors contributed equally to this work.

†ynie@nju.edu.cn

‡wangpeng@nju.edu.cn

(EELS), the atomic-level structural and correlated chemical information of a sample can be routinely obtained [20–23].

In this paper, we directly studied the valence states of both Ti and Fe with an atomic spatial resolution at the interface of the LTO/LFO heterostructure. The heterostructure was grown with atomic-layer precision by reactive molecular beam epitaxy (MBE). We show the existence of interfacial charge transfer from Ti to Fe, and the majority of the transferred charges are located within 1 unit cell from the interface, which is consistent with our density functional theory (DFT) calculations.

II. METHODS

A. Sample growth

The LTO/LFO heterostructure was epitaxially grown on a STO (001) substrate via MBE. The thicknesses of the LTO and LFO layers were 20 and 75 unit cells, respectively. The growth was monitored by *in situ* reflection high-energy electron diffraction (RHEED). On the growth of LFO, the interacting gas consisted of 10% ozone and 90% oxygen, and the oxygen partial pressure was 8.6×10^{-7} Torr. The temperature of the substrate was 721 °C. During the growth of LTO, the interacting gas was changed to a mixture of 10% oxygen and 90% argon. The total pressure and oxygen partial pressure during the growth were 6.2×10^{-7} and 3.4×10^{-8} Torr, respectively, and the substrate temperature was 683 °C.

B. Electron microscopy, EDS, and EELS experiments

The TEM cross-sectional sample was prepared using mechanical thinning, followed by argon ion milling. To remove the amorphous layer, low-energy milling and plasma cleaning were employed. Atomic-resolution HAADF-STEM imaging and EDS elemental mapping were performed using an aberration-corrected FEI Titan G2 60–300 TEM at 300 keV with a field emission gun. The probe convergence angle was 25 mrad, and the angular range of the HAADF detector was from 79.5 to 200 mrad. A Super-X energy dispersive spectrum system with four Si-drifted windowless detectors was used to collect the characteristic x-ray signals, providing the chemical line profile of the structure at atomic resolution. STEM-EELS spectral imaging was performed on a Gatan Quantum 966 system, and the two-dimensional (2D) atomic-level EELS mappings were conducted with the monochromator off. The energy loss near-edge structures (ELNES) were used to study the local electronic structure at a sub-unit-cell resolution using an energy resolution of ~1.2 eV, and the dwell time for recording each spectrum was 0.5 s with a collection semiangle of 36 mrad. In this paper, all EELS spectra were collected in the dual EELS mode and aligned by the zero-loss peak. Data processing of the EELS spectra included pre-edge background subtraction, removal of plural scattering by Fourier-ratio deconvolution, and normalization by integration of the postedge intensity. The thickness of the sample was estimated to be ~22 nm over the field of view using the established EELS log-ratio technique [24].
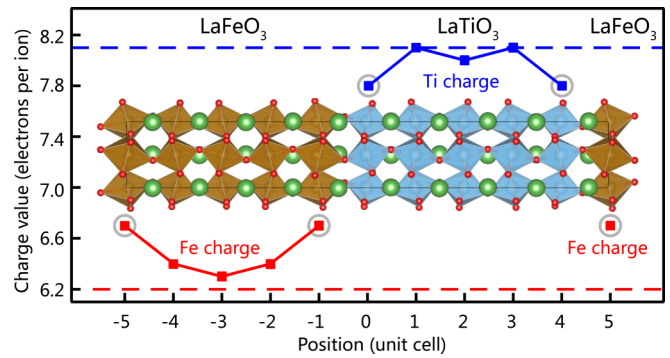

FIG. 1. Calculated Fe/Ti charge in a (5/5) LTO/LFO superlattice. The structure of the superlattice is superposed to illustrate the calculated layer-by-layer charge values. Results from the interfacial layers are marked by gray circles. The red (blue) dashed line indicates the calculated charge of Fe (Ti) in bulk LFO (LTO).

C. Calculation of the Fe valence state

The Fe ELNES L_3/L_2 white-line ratio was calculated by the Pearson method [25]. At each atomic layer, the peak positions of Fe L_2- and L_3-edges were obtained by Gaussian fit. A two-step function was used to model the background intensity caused by the transition to the continuum. The steps were set at the peak positions of Fe L_2- and L_3-edges with a height ratio of 1:2 due to the different transition multiplicity of the $2p$ states [26]. Subsequently, the white-line intensities were integrated in an energy window of 4 eV at each peak position with the continuum background subtracted. The Fe valence state was then converted from the L_3/L_2 white-line ratio using a reference curve from Ref. [26].

D. DFT calculations

To simulate the LTO/LFO interface, we constructed a superlattice that contained five TiO_2 layers and five FeO_2 layers, as shown in Fig. 1. The structure and charge transfer of the superlattice were calculated by DFT in the generalized gradient approximation implemented in the Vienna *ab initio* Simulation Package (VASP) code [27,28], in which the projector augmented wave method [29,30] and the Perdew-Burke-Ernzerhof revised for solids exchange-correlation function (PBEsol) [31] were used. Though a screened hybrid functional would be more powerful in the lattice structure optimization [32–34], the large number of atoms in our superlattice made it beyond our computational capability to adopt the functional. The plane-wave cutoff energy was 520 eV, and the k-mesh was $7 \times 7 \times 1$ for the superlattice. The G-type antiferromagnetic order was used in the calculation with the onsite Coulomb interaction of 4.8 and 3.0 eV for Fe and Ti atoms, respectively [13]. The GdFeO$_3$-type distortions, i.e., rotation and tilt of TiO$_6$ and FeO$_6$ octahedrons, were considered in the superlattice. The in-plane lattice constants of the LTO/LFO superlattice were fixed at the theoretical value of the substrate cubic STO, while the out-of-plane lattice constant and atomic positions were allowed to relax until the residual forces on atoms were <0.02 eV/Å. The charges of Ti and Fe ions were analyzed with the help of the Bader code [35]. We calculated the lattice constants, tilt angles, and rotation
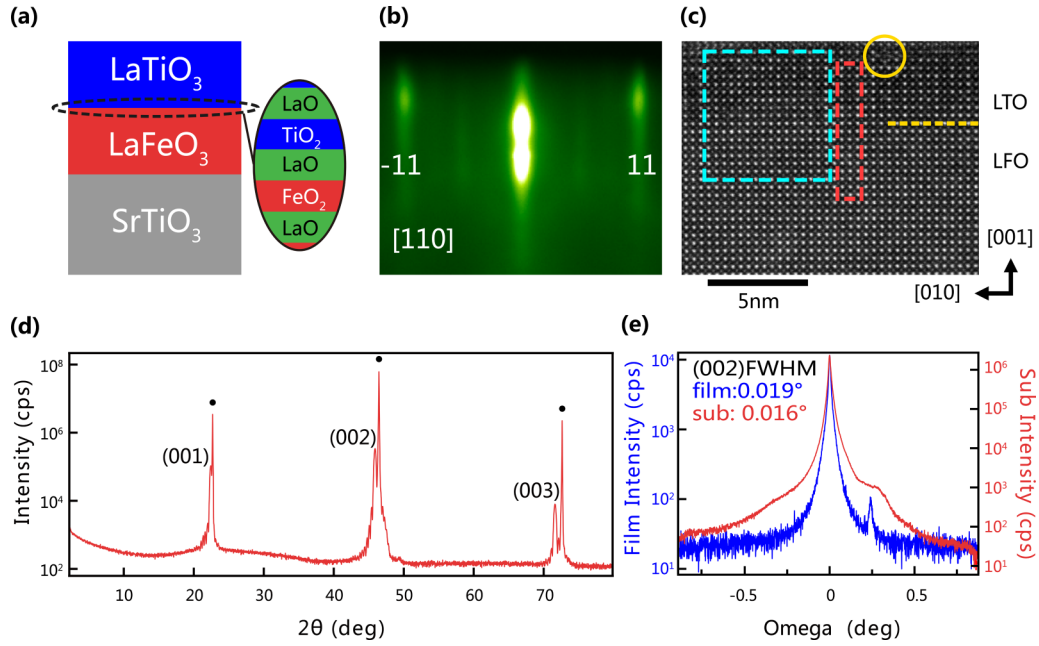
FIG. 2. Structural characterizations of the LTO/LFO heterostructure. (a) Schematic structure of the LTO/LFO heterostructure grown on the STO substrate and the interface configuration. (b) Reflection high-energy electron diffraction (RHEED) pattern of LFO before the growth of LTO. The pattern was taken along the [110] direction, and the first-order diffraction spots are labeled. (c) High-angle annular dark-field (HAADF) image of the heterostructure. The LTO/LFO interface is labeled with the yellow dashed line. The yellow circle points out a type of line defect studied in Ref. [43]. (d) X-ray diffraction (XRD) 2θ-ω patterns. (001), (002), and (003) diffraction peaks of the heterostructure are shown. Peaks marked by solid circles are from the STO substrate. (e) Rocking curves of the film and substrate XRD (002) peaks. The weak peak and shoulder around 0.25 ° are induced by the minor domains of the STO substrate.

angles of bulk LTO, LFO, and STO and made a comparison between the calculated and the experimental results, as shown in Tables SI and SII in the Supplemental Material [36–39]. The comparison shows that the structural parameters calculated by the PBEsol method match well with the experimental results, suggesting that PBEsol is capable of accurately predicting the lattice structure of our system.

III. RESULTS AND DISCUSSION

To investigate the charge transfer at the LTO/LFO interface, we calculated the charge of Fe and Ti ions in their bulk form (LFO or LTO) and in a (5/5) superlattice by DFT calculations using the Bader code [35], and the result is shown in Fig. 1. The Fe (Ti) charge in the bulk form is indicated by the red (blue) dashed line. For the superlattice, we calculated the charge values of Fe or Ti ions in each atomic layer along the alternate stacking direction of the superlattice. The charge values of Fe (Ti) ions away from the interface are like the bulk value, while the ions from the interfacial layer have a higher (lower) charge value. This result suggests possible charge transfer from Ti to Fe at the LTO/LFO interface, and the majority of the charge transfer occurs within 1 unit cell from the interface.

It is worth noting that the charge variation of Fe and Ti is $\sim$0.4 electron, $<$1 electron as expected in the nominal valence model (e.g., change from Fe^{3+} to Fe^{2+}). This is because the bonding between cation and anion is not purely ionic. Even for those classic ionic compounds, like NaCl, the valence state from our calculation using the Bader method is $\pm$0.858, which

is less than the nominal value of $\pm$1 and comparable with the literature [40]. We also calculated the valence states in bulk STO, LFO, and LTO using the Bader code and found all elements showed decreased absolute values of the valence states compared with the nominal valence model, as shown in Table SIV in the Supplemental Material [39].

Additionally, the calculated layer-by-layer tilt and rotation angles of the octahedrons in the LTO/LFO superlattice are shown in Table SIII in the Supplemental Material [39]. Since the in-plane lattice constants of the superlattice are fixed at the theoretical value of the substrate cubic STO, the tilt and rotation angles of the octahedrons in the superlattice have changed slightly from the calculated bulk values. More importantly, the direction and spatial distribution of the charge transfer at the LTO/LFO interface from the calculations are consistent with our experimental results, which will be discussed below.

With a combination of RHEED, x-ray diffraction, and STEM-HAADF, the structural information of the LTO/LFO interface was investigated. LFO and LTO layers were deposited sequentially on a STO substrate by MBE. The atomic configuration of the interface was $LaO-FeO_2-LaO-TiO_2$, which is shown in Fig. 2(a). The RHEED pattern [Fig. 2(b)] taken after the growth of the last FeO_2 layer shows clear first-order diffraction spots and a stripe feature, suggesting that the 2D growth mode occurred at the interface (see also Fig. S1 in the Supplemental Material for the atomic force microscopy image and wider view STEM image of the sample [39]). The x-ray diffraction pattern [Fig. 2(d)] shows (001), (002), and (003) diffraction peaks of the film without any impure peaks. Due to the same lattice structure (space group *Pbnm*)
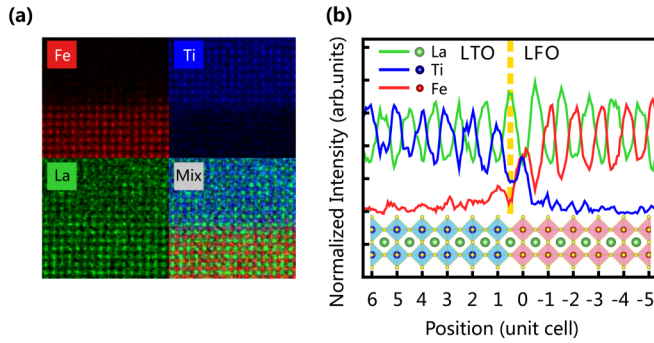
FIG. 3. Energy-dispersive x-ray spectroscopy (EDS) mapping and line profiles of the heterostructure. (a) EDS mapping taken from the cyan dashed line square in Fig. 2(c). The Ti $L_{2,3}$-edge map, Fe $L_{2,3}$-edge map, La $M_{4,5}$-edge map, and mixed color map are shown. (b) Elemental profiles obtained from the EDS maps in panel (a). The yellow dashed line indicates the interface.

and similar lattice constants of LFO [41] ($a = 5.557\,\text{Å}$, $b = 5.5652\,\text{Å}$, and $c = 7.8542\,\text{Å}$) and LTO [42] ($a = 5.615\,\text{Å}$, $b = 7.942\,\text{Å}$, and $c = 5.612\,\text{Å}$), their diffraction peaks overlap with each other and give a c-axis pseudocubic lattice constant of 3.951 Å, which is consistent with the literature [3]. The full width at half maximum (FWHM) of the rocking curves of the film (002) peak and the substrate (002) peak were measured to be $0.019°$ and $0.016°$, respectively. Figure 2(c) shows an atomic-resolution HAADF image of the LTO/LFO heterostructure viewed along the <100> direction, which indicates that a high-quality film was obtained and that no obvious dislocation or defect exists at the interface (marked with a yellow dashed line). However, away from the

interface, we observed a type of line defect introduced by Ref. [43], as marked by the yellow circle in Fig. 2(c). The line defect reflects the existence of Ti and O vacancies in our sample, but the influence on the Ti valence brought by the line defect is limited within the range of the yellow circle with a radius of 1 nm [43]. Hence, the subsequent charge transfer analysis should not be affected by these line defects. Because the HAADF signal is monotonically proportional to the atomic number Z, the contrast of the Fe-O atomic columns was slightly brighter than that of the Ti-O atomic columns due to the higher atomic number of Fe. However, the contrast difference was not large enough to examine the sharpness of the interface. Therefore, atomic-scale EDS elemental mapping was performed to elucidate this matter.

Atomic-resolution EDS mapping [Fig. 3(a)] shows chemical distributions of Ti (blue), Fe (red), and La (green) elements across the LTO/LFO interface, respectively. Figure 3(b) includes the EDS elemental profiles of Ti, Fe, and La extracted from the mappings across the interface. The position of the interface is indicated by a yellow dashed line, and the corresponding structural model is overlaid at the bottom. As shown, both intensity profiles of Ti and Fe extend across the interface by ∼1 unit cell, indicating that minor cation intermixing, which is comparable with other epitaxial works [20,21], takes place at the interfacial layers (unit cell number 0 to 1). As we know from thermodynamics, the high-temperature Ti atoms from the first LTO layer and the Fe atoms from the topmost LFO layer can diffuse into each other's layer during the MBE growth, causing B-site cation intermixing. In addition, the probe broadening of the incident electron beam would also contribute to the intermixed signal [44]. The EDS data show the sharpness of the LTO/LFO interface.
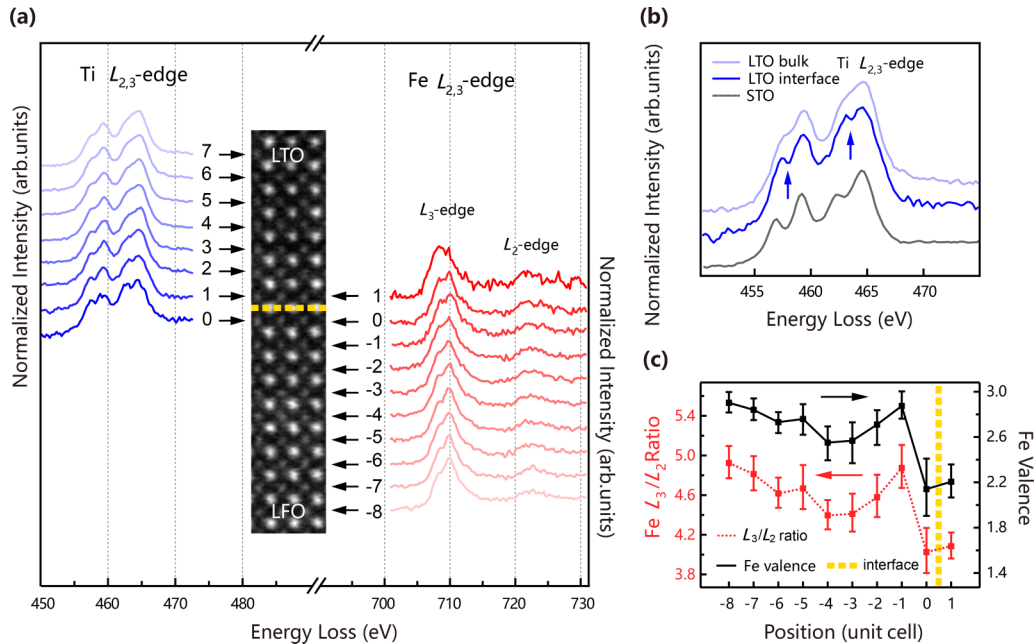

FIG. 4. Energy loss near-edge structures (ELNES) of Ti $L_{2,3}$-edge and Fe $L_{2,3}$-edge near the interface. (a) Normalized Ti $L_{2,3}$-edge and Fe $L_{2,3}$-edge ELNES taken from the dashed red line rectangle in Fig. 2(c). The black arrows point out which layer the corresponding ELNES signal was taken from. (b) The Ti $L_{2,3}$-edge ELNES in the bulk LTO (layer number 6, light blue curve), at the LTO/LFO interface (layer number 1, dark blue curve), and from the STO substrate (gray curve). The blue arrows show the two characteristic dips of Ti^{4+}. (c) Calculated Fe L_3/L_2 ratio and the corresponding Fe valence in each FeO_2 layer from panel (a).

A study of ELNES of the Fe $L_{2,3}$-edge and Ti $L_{2,3}$-edge at the LTO/LFO interface was performed to reveal the layer-by-layer valence state change of the two elements. The spectra of the Ti $L_{2,3}$-edge and Fe $L_{2,3}$-edge acquired from a series of positions across the interface of LTO/LFO are indicated with different colored lines, as shown in Fig. 4(a). Given the previous valence analysis on the Ti $L_{2,3}$-edge [45,46], we observe that the Ti $L_{2,3}$-edge ELNES far from the interface features two peaks, and each peak has a shoulder, showing the Ti^{3+} character. However, four characteristic peaks originated from the splitting of the crystal field are observed near the interface, which indicates the presence of Ti^{4+} at the interfacial atomic layers [typically, the spectral lines from layer number 0 and 1 in Fig. 4(a)]. In addition, signals extracted from layer number 1 and 6, drawn together in Fig. 4(b), clearly show that the dips associated with Ti^{4+} are formed at the interface, which is consistent with the Ti^{4+} ELNES reference taken from the STO substrate. Therefore, the Ti $L_{2,3}$-edge ELNES suggests that the oxidation state of Ti at the interface increases from a lower valence to a higher valence. On the other side, the Fe $L_{2,3}$-edge ELNES appears as two white lines [47], which are derived from the excitation from the $2p_{1/2}$ and $2p_{3/2}$ levels to empty states in the $3d$ band [26,48]. The oxidation state of Fe can be quantified by the L_3/L_2 white-line ratio [Fig. 4(c)], as calculated using the Pearson method [25]. From the result, we notice that the Fe valence state decreases from a higher value in the bulk to a lower value at the interface. From the bulk to the interface, the valence states of Fe and Ti ions change oppositely, indicating that charge transfer from Ti to Fe occurs at the interface. We also measured the Fe valence in the deep LFO layer, and the valence states are like those Fe ions close to the interface (see Fig. S2 in the Supplemental Material [39]).

Since oxygen deficiency is common in oxide heterogeneous systems and it affects the valence states of the transition metals [49–52], the possible influence of oxygen vacancy variation across the interface needs to be evaluated. Therefore, we measured the layer-by-layer O K-edge ELNES spectra over 16 unit cells across the LTO/LFO interface, as shown in Fig. 5. The O K-edge ELNES is originated from the excitation of O $1s$ states to the O $2p$ states hybridized with transition metal states [53] and appears as three featured peaks: a prepeak (peak A) at ∼532 eV, the first main peak (peak B) at ∼535 eV, and the second main peak (peak C) at ∼543 eV. These three peaks can be assigned to the O $2p$ hybridization with $3d$ states of B-site cations Fe or Ti, $5d$ states of the A-site cation La, and $4sp$ states of B-site cations, respectively [53,54]. The prepeak is sensitive to the chemical composition of the B-site cation as well as the bonding features [54,55]. In our LTO/LFO heterostructure, the chemical composition of the B-site cation is changed within the studied region. This explains the difference of the prepeak between LTO and LFO. The difference is weakened by the beam broadening effect and B-site cation intermixing at the LTO/LFO interface, which averages the signals from the LTO and LFO parts. In addition, when the valence state of the B-site cation increases, the prepeak intensity shall be higher since there are more unoccupied O $2p$-Ti $3d$ or O $2p$-Fe $3d$ hybridized states [48,56]. With the increase of the Ti valence state, we expect to observe an increase of the prepeak intensity at the interfacial TiO_2 layers. However, this
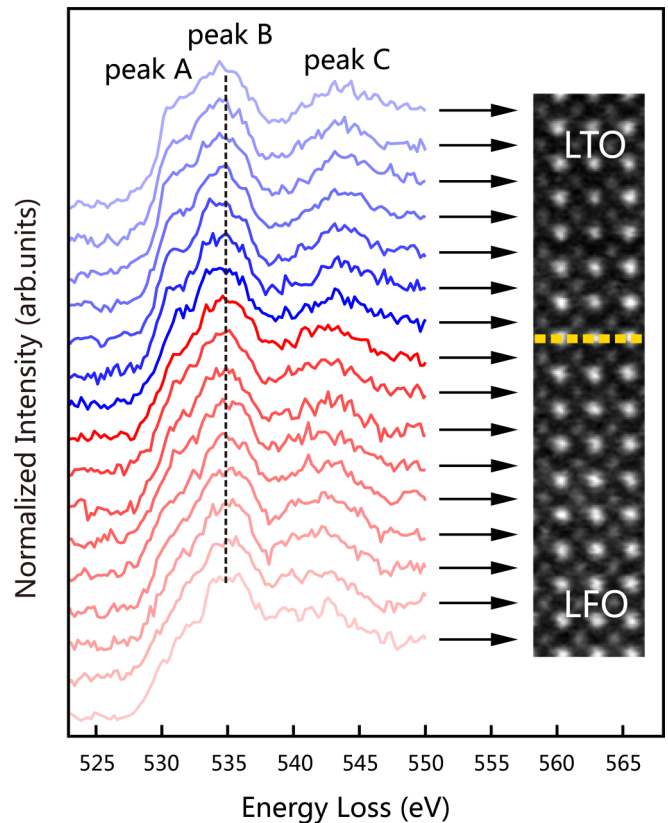

FIG. 5. Oxygen K-edge energy loss near-edge structures (ELNES) fine structure. Three featured peaks are labeled as peaks A, B, and C. The LTO/LFO interface is indicated by the yellow dashed line. The black arrows point out which layer the corresponding ELNES signal was taken from. The black dashed line is for guiding the eyes.

is absent in our experiment. One possible explanation is that the prepeak intensity from LFO is lower than that from LTO, as can be seen from our data, and the probe broadening effect as well as B-site cation intermixing would introduce a signal from LFO. At the interfacial TiO_2 layers, the prepeak intensity increase caused by the Ti valence change is smaller than the intensity decrease caused by the incorporated LFO signal, resulting in the decrease of the overall prepeak intensity. The increase of the prepeak intensity at the interfacial FeO_2 layers can be explained in the same way. Additionally, the position of peak C has a slight shift between LTO and LFO layers, while it rarely changes within each region, which could also be due to the element difference of the B-site cations. Nonetheless, the overall shape of the O K-edge ELNES remains roughly unchanged. According to previous O K-edge ELNES work on a similar perovskite titanate [49], a small number of oxygen vacancies in $SrTiO_{3-\delta}$ ($\delta = 0.13$) can lead to significant shape change of the O K-edge, and the peak B disappears rapidly when δ reaches 0.25, showing a sensitive response to oxygen vacancy. In comparison, the conservation of the peak shape across the interface in our data, especially peak B, suggests that the oxygen content remains nearly unchanged. In other words, the oxygen vacancy does not play a major role in the Fe-Ti charge transfer at the interface.

Our results agree with previous studies, where the charge transfer from Ti to Fe occurs near the LTO/LFO interface, and support the oxygen $2p$ band alignment principle at oxide interfaces [12,13]. In this paper, a complete picture of the charge transfer scenario at the LTO/LFO interface was experimentally shown via the atomic-scale EDS and ELNES studies. The valence change of Ti and Fe ions at the interface were simultaneously observed, and with the oxygen vacancy variation excluded, we suggest that the electrons were transferred from Ti to Fe. It is worth noting that the Fe/Ti intermixing at the LTO/LFO interface may decrease the total charge transfer value, but it does not change the charge transfer physics, as discussed in Ref. [13]. In Fig. 4(c), the valence states of Fe within 1 unit cell from the interface (layer number 0 and 1) are obviously lower than those in other layers. Therefore, the majority of the charge transfer is limited within 1 unit cell from the interface, which is consistent with our DFT results.

IV. CONCLUSIONS

We have synthesized an LTO/LFO heterostructure via MBE and investigated the interface by DFT calculations, aberration-corrected STEM-HAADF, EDS, and EELS. ELNES measurements revealed the valence change of Ti from

Ti^{3+} in the bulk to Ti^{4+} near the interface, which has not been previously observed in the heterostructure. In addition, a valence change of Fe from a high valence state in the bulk to a low valence state near the interface was also observed, suggesting a charge transfer from Ti to Fe near the interface. The major charge transfer in LTO/LFO was determined to be within 1 unit cell from the interface. This paper provides a direct and spatially resolved observation of charge transfer at the LTO/LFO interface, lends significant credence to charge transfer designs in functional oxide interfaces, and the method can be applied to other oxide interfaces.

ACKNOWLEDGMENTS

[1] H. Y. Hwang, Y. Iwasa, M. Kawasaki, B. Keimer, N. Nagaosa, and Y. Tokura, Nat. Mater. **11**, 103 (2012).

[2] D. G. Schlom, L.-Q. Chen, X. Q. Pan, A. Schmehl, and M. A. Zurbuchen, J. Am. Ceram. Soc. **91**, 2429 (2008).

[3] A. Ohtomo, D. A. Muller, J. L. Grazul, and H. Y. Hwang, Nature **419**, 378 (2002).

[4] J. Biscaras, N. Bergeal, S. Hurand, C. Grossetête, A. Rastogi, R. C. Budhani, D. LeBoeuf, C. Proust, and J. Lesueur, Phys. Rev. Lett. **108**, 247004 (2012).

[5] M. Gibert, P. Zubko, R. Scherwitzl, J. Íñiguez, and J.-M. Triscone, Nat. Mater. **11**, 195 (2012).

[6] K. Ueda, H. Tabata, and T. Kawai, Science **280**, 1064 (1998).

[7] A. Ohtomo and H. Y. Hwang, Nature **427**, 423 (2004).

[8] T. D. N. Ngo, J.-W. Chang, K. Lee, S. Han, J. S. Lee, Y. H. Kim, M.-H. Jung, Y.-J. Doh, M.-S. Choi, J. Song, and J. Kim, Nat. Commun. **6**, 8035 (2015).

[9] L. Li, C. Richter, J. Mannhart, and R. C. Ashoori, Nat. Phys. **7**, 762 (2011).

[10] E. Pavarini, S. Biermann, A. Poteryaev, A. I. Lichtenstein, A. Georges, and O. K. Andersen, Phys. Rev. Lett. **92**, 176403 (2004).

[11] C. A. L. Dixon, C. M. Kavanagh, K. S. Knight, W. Kockelmann, F. D. Morrison, and P. Lightfoot, J. Solid State Chem. **230**, 337 (2015).

[12] Z. Zhong and P. Hansmann, Phys. Rev. X **7**, 011023 (2017).

[13] J. E. Kleibeuker, Z. Zhong, H. Nishikawa, J. Gabel, A. Müller, F. Pfaff, M. Sing, K. Held, R. Claessen, G. Koster, and G. Rijnders, Phys. Rev. Lett. **113**, 237402 (2014).

[14] A. Ohtomo, D. A. Muller, J. L. Grazul, and H. Y. Hwang, Appl. Phys. Lett. **80**, 3922 (2002).

[15] T. T. Zhang, C. Y. Gu, Z. W. Mao, X. F. Chen, Z. B. Gu, P. Wang, Y. F. Nie, and X. Q. Pan, Appl. Phys. Lett. **115**, 261604 (2019).

[16] P. E. Batson, N. Dellby, and O. L. Krivanek, Nature **418**, 617 (2002).

[17] M. Haider, S. Uhlemann, E. Schwan, H. Rose, B. Kabius, and K. Urban, Nature **392**, 768 (1998).

[18] J. Miao, T. Ohsuna, O. Terasaki, K. O. Hodgson, and M. A. O'Keefe, Phys. Rev. Lett. **89**, 155502 (2002).

[19] P. Wang, A. L. Bleloch, M. Falke, and P. J. Goodhew, Appl. Phys. Lett. **89**, 072111 (2006).

[20] S. R. Spurgeon, P. V. Sushko, S. A. Chambers, and R. B. Comes, Phys. Rev. Mater. **1**, 063401 (2017).

[21] P. Xu, W. Han, P. M. Rice, J. Jeong, M. G. Samant, K. Mohseni, H. L. Meyerheim, S. Ostanin, I. V. Maznichenko, I. Mertig, E. K. U. Gross, A. Ernst, and S. S. P. Parkin, Adv. Mater. **29**, 1604447 (2017).

[22] W. Huang, Y. Yin, and X. Li, Appl. Phys. Rev. **5**, 041110 (2018).

[23] T. C. Kaspar, P. V. Sushko, S. R. Spurgeon, M. E. Bowden, D. J. Keavney, R. B. Comes, S. Saremi, L. Martin, and S. A. Chambers, Adv. Mater. Interfaces **6**, 1801428 (2019).

[24] D. A. Muller, L. F. Kourkoutis, M. Murfitt, J. H. Song, H. Y. Hwang, J. Silcox, N. Dellby, and O. L. Krivanek, Science **319**, 1073 (2008).

[25] D. H. Pearson, C. C. Ahn, and B. Fultz, Phys. Rev. B **47**, 8471 (1993).

[26] H. K. Schmid and W. Mader, Micron **37**, 426 (2006).

[27] G. Kresse and J. Furthmüller, Comput. Mater. Sci. **6**, 15 (1996).

[28] G. Kresse and J. Furthmüller, Phys. Rev. B **54**, 11169 (1996).

[29] P. E. Blöchl, Phys. Rev. B **50**, 17953 (1994).

[30] G. Kresse and D. Joubert, Phys. Rev. B **59**, 1758 (1999).

[31] J. P. Perdew, A. Ruzsinszky, G. I. Csonka, O. A. Vydrov, G. E. Scuseria, L. A. Constantin, X. Zhou, and K. Burke, Phys. Rev. Lett. **100**, 136406 (2008).

[32] S. Jana, B. Patra, S. Śmiga, L. A. Constantin, and P. Samal, Phys. Rev. B **102**, 155107 (2020).

[33] S. Jana, A. Patra, L. A. Constantin, and P. Samal, J. Chem. Phys. **152**, 044111 (2020).

[34] F. El-Mellouhi, E. N. Brothers, M. J. Lucero, I. W. Bulik, and G. E. Scuseria, Phys. Rev. B **87**, 035107 (2013).

[35] W. Tan, E. Sanville, and G. Henkelman, J. Phys.: Condens. Matter **21**, 084204 (2009).

[36] M. Marezio and P. D. Dernier, Mater. Res. Bull. **6**, 23 (1971).

[37] M. Capone, C. J. Ridley, N. P. Funnell, M. Guthrie, and C. L. Bull, Phys. Status Solidi B **258**, 2000413 (2021).

[38] M. Cwik, T. Lorenz, J. Baier, R. Müller, G. André, F. Bourée, F. Lichtenberg, A. Freimuth, R. Schmitz, E. Müller-Hartmann, and M. Braden, Phys. Rev. B **68**, 060401(R) (2003).

[39] See Supplemental Material at http://link.aps.org/supplemental/10.1103/PhysRevB.104.085115 for additional DFT and experimental results.

[40] M. Yu and D. R. Trinkle, J. Chem. Phys. **134**, 064111 (2011).

[41] J. W. Seo, E. E. Fullerton, F. Nolting, A. Scholl, J. Fompeyrine, and J.-P. Locquet, J. Phys.: Condens. Matter **20**, 264014 (2008).

[42] C. Eylem, Y.-C. Hung, H. L. Ju, J. Y. Kim, D. C. Green, T. Vogt, J. A. Hriljac, B. W. Eichhorn, R. L. Greene, and L. Salamanca-Riba, Chem. Mater. **8**, 418 (1996).

[43] J. S. Jeong, M. Topsakal, P. Xu, B. Jalan, R. M. Wentzcovitch, and K. A. Mkhoyan, Nano Lett. **16**, 6816 (2016).

[44] N. Nakagawa, H. Y. Hwang, and D. A. Muller, Nat. Mater. **5**, 204 (2006).

[45] L. Fitting, S. Thiel, A. Schmehl, J. Mannhart, and D. A. Muller, Ultramicroscopy **106**, 1053 (2006).

[46] Z. Zhang, W. Sigle, and W. Kurtz, Phys. Rev. B **69**, 144103 (2004).

[47] R. D. Leapman and L. A. Grunes, Phys. Rev. Lett. **45**, 397 (1980).

[48] C. Colliex, T. Manoubi, and C. Ortiz, Phys. Rev. B **44**, 11402 (1991).

[49] D. A. Muller, N. Nakagawa, A. Ohtomo, J. L. Grazul, and H. Y. Hwang, Nature **430**, 657 (2004).

[50] Z. Li, M. Bosman, Z. Yang, P. Ren, L. Wang, L. Cao, X. Yu, C. Ke, M. B. H. Breese, A. Rusydi, W. Zhu, Z. Dong, and Y. L. Foo, Adv. Func. Mater. **22**, 4312 (2012).

[51] H. O. Moltaji, J. P. Buban, J. A. Zaborac, and N. D. Browning, Micron **31**, 381 (2000).

[52] Z. Yuan, J. Ruan, L. Xie, X. Pan, D. Wu, and P. Wang, Appl. Phys. Lett. **110**, 171602 (2017).

[53] A. B. Shah, Q. M. Ramasse, X. Zhai, J. G. Wen, S. J. May, I. Petrov, A. Bhattacharya, P. Abbamonte, J. N. Eckstein, and J.-M. Zuo, Adv. Mater. **22**, 1156 (2010).

[54] A. Gloter, J. Ingrin, D. Bouchet, and C. Colliex, Phys. Rev. B **61**, 2587 (2000).

[55] M. Varela, M. P. Oxley, W. Luo, J. Tao, M. Watanabe, A. R. Lupini, S. T. Pantelides, and S. J. Pennycook, Phys. Rev. B **79**, 085117 (2009).

[56] A. S. Sefat, G. Amow, M.-Y. Wu, G. A. Botton, and J. E. Greedan, J. Solid State Chem. **178**, 1008 (2005).